Available online at www.sciencedirect.com
SCIENCE DIRECT®
Optics Communications 222 (2003) 17–28
OPTICS COMMUNICATIONS
www.elsevier.com/locate/optcom

Fluorescence of a highly collimated atomic cesium beam: theory and experiment

Vladislav Gerginov, Carol E. Tanner*

Department of Physics, College of Science, University of Notre Dame, 225 Nieuwland Science Hall, Notre Dame, IN 46556-5670, USA

Received 17 February 2003; received in revised form 18 April 2003; accepted 6 May 2003

Abstract

We describe our system for producing a dense well collimated atomic cesium beam. Our motivation for constructing this system is to perform high resolution laser induced spectroscopy. The two stage oven system consists of a nozzle and reservoir. An array of stainless steel capillary tubes forms the exit port of the nozzle. Additional collimation of the atomic beam is achieved with a stack of microscope cover slips and spacers, giving a maximum beam divergence of 13.6 mrad. The heterodyne beat note between two diode lasers provides the frequency calibration for high resolution fluorescence spectra. Fluorescence spectra with high signal to noise ratio are accurately described by a simple theoretical model that gives a residual Doppler width of 2.3(1) MHz in agreement with the geometrical constraints of the collimator.

PACS: 32.10.Fn; 32.70.Jz; 39.10.+j; 42.55.Px; 42.62.Fi

Keywords: Hyperfine structure; Line shapes; Atomic beam; Laser diodes; Laser spectroscopy

1. Introduction

Our motivation for constructing this thermal beam system involves the spectroscopy of the low lying electronic states of ^{133}Cs which are shown in Fig. 1 along with the corresponding hyperfine splittings (HFS). The experiment in progress is the precise measurement of the Cs 6p $^2P_{3/2}$ state hyperfine splittings. With the atomic beam described here and the laser system described else where [1], we can acquire well calibrated fluorescence spectra from which we can determine the splittings to a precision of a few kHz. This precision is about an order of magnitude better than the most accurate previous results [2]. From measurements of these hyperfine splittings, one can determine the strength of the magnetic dipole, electric quadrupole, and magnetic octupole interactions between the nucleus and the orbital electrons [3]. When our measurements are complete, we expect the results will provide tests for theories of atomic and nuclear structure. In this

* Corresponding author. Tel.: +1-219-631-8369; fax: +1-219-631-5952.
E-mail address: carol.e.tanner.1@nd.edu (C.E. Tanner).

0030-4018/03/$ - see front matter
doi:10.1016/S0030-4018(03)01505-0

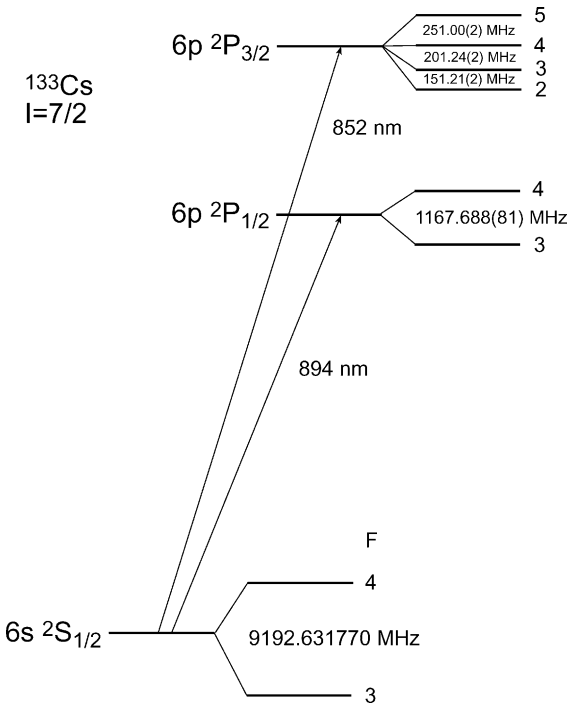

Fig. 1. Shown are the low lying electronic states of atomic cesium with hyperfine intervals [2,11,12] and rest frame transition wavelengths.

paper, we describe our thermal atomic beam system and the lineshape model we use to fit the high resolution fluorescence spectra obtained by laser excitation.

2. Thermal atomic beam

The high resolution spectra presented here require a dense and well collimated atomic beam. The cesium oven comprises a nozzle and a reservoir as shown in Fig. 2. The nozzle is constructed of a stainless steel vessel surrounded by heaters. Atomic cesium vapor effuses from the exit port of the nozzle through an array of closely packed stainless steel tubes. The cesium reservoir is constructed of commercial stainless steel vacuum components with knife edge seals. A metal seal bellows valve between the reservoir and the nozzle allows the reservoir to be sealed off under vacuum before opening the chamber to air. The valve and reservoir are wrapped in heater tape with the valve kept hotter than the cesium reservoir. During normal operations, the entire nozzle region is kept at a temperature of 170 °C while the cesium reservoir is kept at 110 °C. This temperature provides enough atomic density in the beam while keeping the background level of Cs within the capability of the pumping system to prevent the formation of a cloud. The vacuum with the beam running is 1×10^{-6} Torr. The beam passes through a collimator which restricts its divergence in the horizontal plane. The final density of the beam is approximately 3×10^{13} cm^{-3}.

2.1. Stainless steal array

We have constructed a robust oven nozzle for Cs vapor using a closely packed array of 21 gauge thin wall stainless steel tubing 0.032 in. OD × 0.023 in. ID (Small Parts model HTX-21-12TW HYPO Tube 304

stainless steel). The tubes were roughly cut to a length slightly longer that 1 cm with a small grinding tool. A mini conflat flange with a 5×15 mm rectangular hole forms the supporting body of the array. The hole in the flange is filled with tubes until the tubes are jammed tightly into a closely backed bundle. The tubes and spaces between tubes form narrow channels. Around the edges of the hole some channels are not as long as 1 cm because the conflat flange is not that thick. Torr Seal vacuum epoxy is used to fill these gaps which also helps to hold the outer most tubes in place. The tubes filling the hole do not form a perfect closely packed lattice, but that does not seem to matter. A small grinding tool was used to even up the ends of the tubes on the outside and inside of the flange to a final length of about 1 cm. The inside and outside array facets were polished with fine emery paper to remove burrs from the tube ends. As opposed to micro channel plate glass capillary arrays [4], this nozzle is not easily clogged or attacked by Cs vapor.

2.2. Collimator

External to the nozzle array, we place a collimator constructed of microscope cover slips 12 cm away from the nozzle array. The collimator is made of #1 ($0.170 \times 25 \times 25$ mm) glass microscope cover slips stacked together with pieces of cover slips as spacers in an aluminum frame and glued together with cyanoacrylate glue that wicks into the edges of the stack. We also apply epoxy to the edges for added strength. The atomic beam profile after the collimator has a rectangular shape, 13 mm wide and 15 mm high. The collimator geometrically restricts the atomic beam to a maximum possible full divergence angle of 13.6 mrad in the horizontal plane. Fitting the spectra indicates that Doppler broadening due to beam divergence is 2.3(1) MHz which is consistent with our expectations based on the geometrical constraints. The collimator stays at room temp, but never clogs. It is mounted on a motorized piezo two-axis tilting stage for fine alignment along the thermal beam axis. We have also made a collimator out of cover slips spaced with pieces of 1 mm thick microscope slides, which produces a denser atomic beam but its divergence is larger. These collimators do not seem to be attacked or damaged by the Cs vapor.

2.3. Oven

The nozzle, array and valve are always kept warmer than the Cs reservoir to keep metallic Cs from condensing in places other than the reservoir. To prevent clogging, we always keep the nozzle hotter than the Cs reservoir. When not in use, but still under vacuum the nozzle is always kept about 10 °C warmer than room temperature. The Cs reservoir is in a section of the vacuum system that can be sealed under vacuum with the metal seal bellows valve before the rest of the chamber is opened to the air. The reservoir is constructed from a conflat T that holds a Cs ampule and is attached to a mini conflat metal seal valve that is wrapped in heater tape. The temperature of the conflat T is kept lower than all the other oven parts so that Cs condenses only in the ampule. A schematic of the oven is shown in Fig. 2.

3. Fluorescence signal collection system

The Cs beam passes through the collimator then above a large area photo detector with 25 mm diameter. A 5 mm diameter laser beam with intensity on the order of 1 $\mu W/cm^2$ crosses the thermal beam in the perpendicular direction. The laser beam is linearly polarized along the thermal beam axis. The fluorescence which escapes in the vertical plane is reflected with a curved gold-coated plastic mirror (10 cm radius of curvature) to enhance the signal on the photodiode. The mirror is mounted on a copper ring above the photo detector, with the distance between the mirror and the photo detector determined by the vertical dimension of the atomic beam. The copper ring has openings for passage of the laser beam and the atomic beam. The ring acts as a shield to reduce the amount of scattered light from the chamber input and output

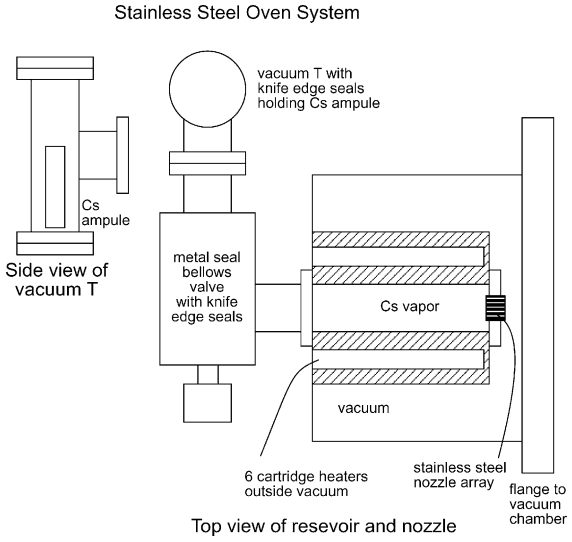

Fig. 2. Cesium oven diagram. All vacuum flanges exposed to Cs have knife edge seals with copper gaskets. The flange to the chamber has an o-ring.

windows without introducing a stray magnetic field. The photo detector is connected with a coaxial cable to a coaxial vacuum feedthrough, and then to a very high gain photo detector amplifier. The amplifier is based on LF356N Operational Amplifier and has 1.23 GΩ feedback resistor in parallel with a 2 pF mica capacitor. The amplifier integrates any fast signal changes above 1 kHz and cannot tolerate rapid signal changes without distortion. We use it mostly in a DC regime with the laser induced fluorescence kept at a fixed level and average with a data acquisition (DAQ) board that reads the amplifier output voltage directly. The fluorescence signal is typically several hundred mV. The photo detector-amplifier system has a 15 mV AC noise modulation at 60 Hz, which we eliminate with signal averaging. It can register extremely low light intensities and replaces bulky photo multipliers. The transmitted laser light is monitored with a 10 mm diameter photo detector with similar amplifier employing a feedback resistor of 10 MΩ in parallel with a 2 pF mica capacitor. By also recording transmission, we are able to determine the laser intensity, the size of the thermal Cs cloud, and the atomic beam density. Both fluorescence and transmission signals are read with a PCI-MIO-16XE-10 100 kS/s, 16-Bit, Analog input Multifunction DAQ board from National Instruments, and controlled with a Labview based program. The DAQ board characteristics are 0.0044%/24 h absolute accuracy, 479.2 μV offset and relative accuracy resolution of 723.3 μV between two measurements. With our noise level, these contributions from the board are completely negligible.

4. Thermal beam modeling

4.1. Fluorescence functional form

The atomic beam is modeled by assuming that Cs atoms effuse through a small aperture and that a laser excites the beam in a perpendicular direction at distance L from the aperture, as shown in Fig. 3. If the aperture is considered small, the oven creates conditions for thermal equilibrium of the atomic velocities, giving a Maxwell–Boltzmann distribution in the nozzle. The total number of atoms in a volume $A\cos\theta\,dr$ effusing through the small aperture of area A with a velocity between $V, V + dV$, at an angle θ, in solid angle $d\Omega$ is given by

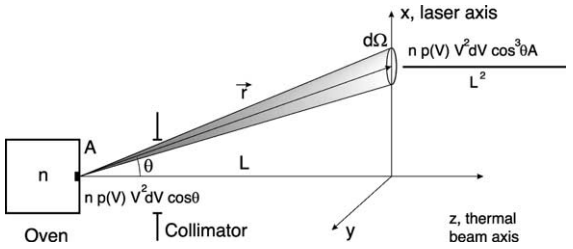

Fig. 3. Thermal beam angular dependence and coordinate system for derivation of formulae.

$$\text{No. of atoms} = np(V)V^2\mathrm{d}V\mathrm{d}\Omega(A\cos\theta\,\mathrm{d}r), \tag{1}$$

where n is the vapor density in the nozzle, $p(V)$ is the thermal velocity distribution, and θ is the angle between the exciting velocity direction and the direction defined as a beam propagation axis. At a distance L from the aperture measured along the atomic beam direction of propagation z, the density of atoms is found by dividing the number of atoms by the differential volume $r^2\mathrm{d}\Omega\,\mathrm{d}r$ at a distance r from the aperture where $r = L/\cos\theta$. So the effective density of these atoms at the place of interaction with the laser beam is

$$\mathrm{d}N_{V,\theta} = n\frac{A}{L^2}p(V)V^2\mathrm{d}V\cos^3\theta. \tag{2}$$

In our system, the angle θ is restricted by the collimator placed in the atomic beam downstream of the nozzle.

The laser electric field attenuation coefficient versus the distance along the laser beam direction of propagation x due to the presence of absorbing atoms of density n is given by [5]

$$\alpha_{\pm1} = n\pi\alpha\omega_\gamma\sum_{eg}\frac{\Gamma_e}{g_g}\frac{|\langle e|r_{\pm1}|g\rangle|^2}{(\omega_{eg}-\omega_\gamma)^2+\Gamma_e^2/4}, \tag{3}$$

where α is the fine structure constant, ω_γ is the laser frequency in radians, Γ_e is the excited state natural linewidth in radians per unit time, g_g is the ground state degeneracy, ω_{ge} is the level separation frequency in radians per unit time, $|\langle e|r_{\pm1}|g\rangle|^2$ is the radial matrix element for electric dipole transitions written in terms of spherical tensor components, and $|g\rangle$, $|e\rangle$ are the ground and excited state wave functions. The ±1 stands for left and right circularly polarized light. The fluorescence of the atoms excited by the laser is proportional to the attenuation of the laser field intensity. With the approximation of small attenuation and zero magnetic field (α_{+1} equals α_{-1}), the laser intensity change is equal to

$$I(x) - I(0) = I(0)\left(1-\mathrm{e}^{(-2\alpha_{\pm1}x)}\right) \approx 2I(0)\alpha_{\pm1}x, \tag{4}$$

where x equals the path length of the laser through the atoms and $I(0)$ is the incident laser intensity. In order to include the spread of atomic velocities, the laser frequency must be Doppler shifted into the rest frame of the moving atom. When all possible atomic velocities, directions of propagation and angles are included, the resulting frequency dependent fluorescence signal produced per unit volume is given by

$$F(\omega_\gamma) = 2I(0)\left[n\left(\frac{A}{L^2}\right)\right]\pi\alpha\omega_\gamma \times\sum_{eg}\left\{\frac{\Gamma_e}{g_g}|\langle e|r_{\pm1}|g\rangle|^2\left[\left(\frac{M}{2\pi kT}\right)^{3/2}\times\int_{\theta_1}^{\theta_2}\int_0^\infty\frac{\mathrm{e}^{-\frac{MV^2}{2kT}}V^2\mathrm{d}V\cos^3\theta\,\mathrm{d}\theta}{\left[\omega_\gamma-\omega_{eg}\left(1+\frac{V}{c}\sin\theta\right)\right]^2+\Gamma_e^2/4}\right]\right\}, \tag{5}$$

where M is the mass of the atom, k is the Bolzmann constant, T is the oven temperature in K, $\Delta\omega_D = 2\omega_{eg}/c\sqrt{2kT\ln 2/M}$ is the Doppler width. When $\theta_2 = -\theta_1 = \theta_c$ the maximum angle allowed by the collimator, then the atomic beam is exactly perpendicular to the laser beam. The assumption of small angles

for θ allows us to approximate the $\cos^3\theta$ term with 1. Using a change of variables $\omega' = \omega_{eg}\left(1 \pm \frac{V}{c}\sin\theta\right)$ to express the velocity V in terms of Doppler shifted level separation frequency ω', with the sign depending on the sign of θ, the frequency dependent fluorescence signal becomes

$$F(\omega_\gamma) = 2I(0)\left[n\left(\frac{A}{L^2}\right)\right]\pi\alpha\omega_\gamma \sum_{eg}\left\{\frac{\Gamma_e}{g_g}|\langle e|r_{\pm 1}|g\rangle|^2\left[\frac{1}{2\pi^{3/2}}\left(\frac{2\sqrt{\ln 2}}{\Delta\omega_D}\right)\int_{-\infty}^{\infty}\frac{e^{-[(\omega'-\omega_{eg})2\sqrt{\ln 2}/\Delta\omega'_D]^2}d\omega'}{(\omega_\gamma-\omega')^2+\Gamma_e^2/4}\right]\right\}. \tag{6}$$

Assuming ω_γ to be much bigger than $\omega_\gamma - \omega_{eg}$, the frequency dependent part is the usual expression for a Voigt profile. Similar results can be found in [6,7]. Eq. (6) differs from the vapor cell absorption expression only by the reduced Doppler width given here by $\Delta\omega'_D = \Delta\omega_D\theta_c$, which for small collimator angles is much smaller than the Doppler width in a cell (on the order of $2\pi \times 460$ MHz at the oven temperature).

4.2. Laser-atomic beam misalignment

Obtaining the Voigt profile in Eq. (6) depends on having exact symmetry of integration between the positive and negative allowed angles. Such perfect alignment is not necessarily easy to achieve, especially in a well collimated atomic beam. We have also considered the possibility that the laser beam is not exactly perpendicular to the atomic beam. If we take the angles θ_1 and θ_2 in Eq. (5) to be the minimum and maximum angles that the atomic velocities can make with the laser beam direction, then the fluorescence signal is proportional to:

$$F(\omega_\gamma) \sim \left(\frac{1}{\pi}\right)^{3/2}\left(\frac{2\sqrt{\ln 2}}{\Delta\omega_D}\right)^3\left\{\int_{\omega_{eg}}^{\infty}\frac{(\omega'-\omega_{eg})^2}{(\omega_\gamma-\omega')^2+\Gamma_e^2/4}I_+\,d\omega' + \int_{-\infty}^{\omega_{eg}}\frac{(\omega'-\omega_{eg})^2}{(\omega_\gamma-\omega')^2+\Gamma_e^2/4}I_-d\omega'\right\},$$

$$I_+ = \begin{cases} I(\theta_2) - I(\theta_1): & \theta_2 > \theta_1 > 0 \\ I(\theta_2): & \theta_2 > 0, \theta_1 < 0 \\ 0: & \theta_1 < \theta_2 < 0 \end{cases}$$

$$I_- = \begin{cases} 0: & \theta_2 > \theta_1 > 0 \\ I(\theta_1): & \theta_2 > 0, \theta_1 < 0 \\ I(\theta_2) - I(\theta_1): & \theta_1 < \theta_2 < 0 \end{cases} \tag{7}$$

where $I(\theta_1)$ and $I(\theta_2)$ are defined through

$$\begin{aligned} I(\theta) &= \int_0^\theta \frac{e^{-[(\omega'-\omega_{eg})2\sqrt{\ln 2}/\Delta\omega_D\sin\theta']^2}}{\sin^3\theta'}\cos^3\theta'\,d\theta' \\ &= \frac{1}{2}\frac{e^{-[(\omega'-\omega_{eg})2\sqrt{\ln 2}/\Delta\omega_D\sin\theta]^2}}{[(\omega'-\omega_{eg})2\sqrt{\ln 2}/\Delta\omega_D]^2} - \frac{1}{2}\Gamma\left(0, \left[\frac{(\omega'-\omega_{eg})2\sqrt{\ln 2}}{\Delta\omega_D\sin\theta}\right]^2\right) \end{aligned} \tag{8}$$

where $\Gamma(a,z) = \int_z^\infty t^{a-1}e^{-t}\,dt$ is the incomplete Gamma function. The fluorescence functional form includes the Doppler shifts of the line center due to the finite angle between the atomic beam and the laser beam and works for atomic beam collimating angles that are not necessarily small. For small angles $\theta_{1,2}$

the contribution coming from the second term in Eq. (9) can be neglected. If also $\theta_1 \equiv \theta_2$ (symmetric case) the formula gives the Voigt profile described in the previous section.

4.3. Fitting model

Due to the ^{133}Cs nuclear spin $I = 7/2$ there are many Zeeman substates belonging to each hyperfine level. To reduce the number of parameters in the model and the calculation time, several simplifications are made. We work at zero magnetic field where the Zeeman substates overlap, and their absorption is given by a sum of functionally equivalent Voigt profiles with amplitudes determined by the angular momentum parts of the transition probability. Experimentally this requires nulling the Earth's magnetic field. We also assume that the population of Zeeman substates belonging to a single hyperfine level are equal. To achieve this condition, we keep the excitation laser intensities low (on the order of 1 μW/cm^2) to avoid optical pumping. For the case 6s $^2S_{1/2} \rightarrow$ 6p $^2P_{3/2}$, there are three allowed transitions from each ground state hyperfine level. These levels are separated by 9.2 GHz, which allows the narrow laser to resolve each level. Spectra are taken that include all three excited state transitions from each ground state level. Typical spectra are shown in Figs. 4 and 5.

The Doppler width of the profiles is the same for all three transitions and is used as a fit parameter. Each peak height and its Lorentzian width is allowed to vary. To account for a possible thermal cloud inside the chamber and its contribution to the spectra, a thermally broadened Doppler profile is also included for each transition. The amplitude of the cloud profile for each peak is proportional to the corresponding transition probability. The proportionality factor is kept the same for all three lines. The Doppler width of the cloud is a chosen parameter set equal to the hottest point in the vacuum system (the oven kept at 170 °C). The laser transmission through the chamber is recorded together with the fluorescence signal, and is used as an independent check for a possible thermal background. Due to the geometry, the path of the laser through the cloud is $\sim$12 times longer than through the beam. The actual amplitude of the Doppler broadened background in the transmission spectra is compared with its amplitude found from the fit of the fluorescence

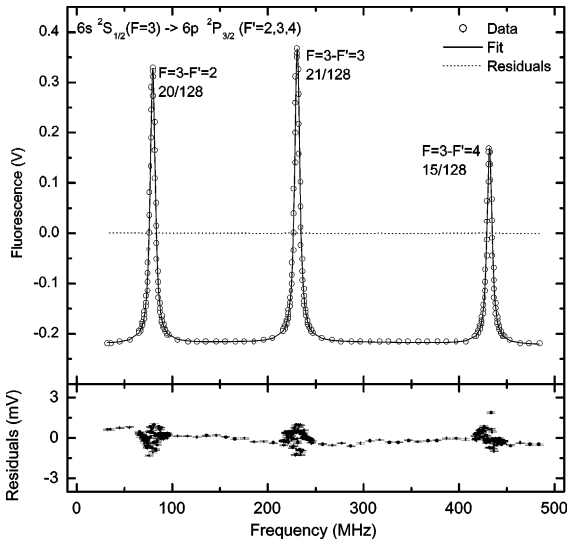

Fig. 4. Plot of the thermal beam fluorescence spectrum with excitation laser starting from F = 3 ground state. The laser frequency difference is scanned by setting the RF oscillator at specific frequencies. The averaged Cs fluorescence is represented with circles. Relative theoretical heights are also shown. The solid line is the theoretical fit. The dashed line represents the residuals. The bottom trace shows the residuals magnified, with the uncertainty for each fluorescence point shown as an error bar.

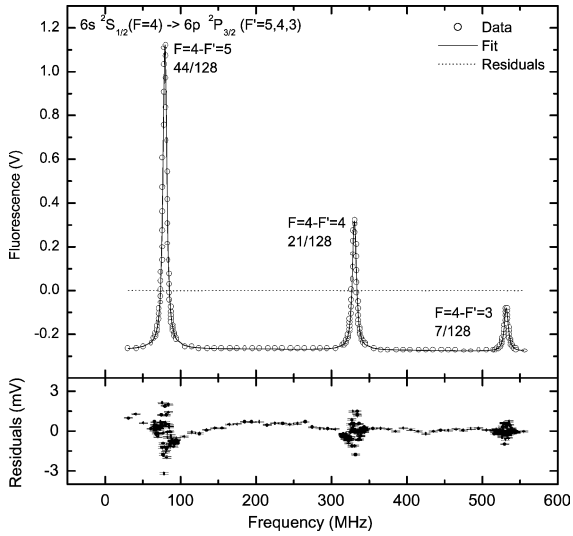

Fig. 5. Plot of the thermal beam fluorescence spectrum with excitation laser starting from F = 4 ground state. The laser frequency difference is scanned by setting the RF oscillator at specific frequencies. The averaged Cs fluorescence is represented with circles. Relative theoretical heights are also shown. The solid line is the fit. The dashed line represents the residuals. The bottom trace shows the residuals magnified, with the uncertainty for each fluorescence point shown as an error bar.

spectra. A constant and linear background are also included in the fit, although it was found that the linear background part is always negligible.

The linear background might be expected due to the 0.3% change of the laser intensity over the entire scan, but is found to be too small to be observed since the amount of scattered laser light hitting the photo detector is negligible. The laser intensity change is not included into the functional form of the line profile because it is negligibly small for frequency intervals of the order of these peak widths. The amplified reverse voltage of the photo detector adds to the amplifier output signal and is responsible for the negative constant background of all the spectra. Temperature changes can slowly alter this reverse voltage. In our case, the photo detector is placed inside the vacuum chamber on a plastic mount and its temperature does not change over the time of a single scan. However, the linear background could account for a possible linear drift in this voltage.

Using the Levenberg–Marquardt nonlinear fitting method is taken from [8]. The frequency dependence of the amplitude-normalized Voigt profile is given by the following formula:

$$V(\omega_\gamma) = \left(\frac{\Delta\omega_L}{2}\right) \frac{e^{-(\Delta\omega_L\sqrt{\ln 2}/\Delta\omega'_D)^2}}{\pi[1 - Erf(\Delta\omega_L\sqrt{\ln 2}/\Delta\omega'_D)]} \int_0^\infty \frac{e^{-[(\omega'-\omega_{eg})2\sqrt{\ln 2}/\Delta\omega'_D]^2} d\omega'}{(\omega_\gamma - \omega')^2 + \Delta\omega_L^2/4} \tag{9}$$

where $Erf(x)$ is the error function. Instead of the usual numerical approximation [9] we use a direct numerical integration of the function $V(\omega)$ and its partial derivatives for each value of ω. On a 450 MHz Pentium III computer, the fit of a three peak spectrum consisting of 250 data points usually takes around 30 s to converge.

5. Measurement protocol

The laser system used to excite the 6p $^2P_{3/2}$ state in Cs and to calibrate the laser frequency detuning is described in detail in [1]. The reference laser is narrowed using optical feedback from a Faraday filter in an

external cavity configuration. Its frequency is also locked to a saturated absorption signal in a Cs cell using sideband technique similar to [10], leaving the main laser output unaltered. The scanning laser is narrowed with optical feedback from a confocal Fabry–Perot cavity and its frequency can be scanned over several hundred MHz. Parts of each laser output beam are combined on a fast photo detector providing a beat note signal measured with a frequency counter. Both lasers have linewidths of the order of 50 kHz as measured from the beat note spectrum. Part of the beat note signal is used to lock the laser frequency difference to a stable RF oscillator. By changing the oscillator frequency, the scanning laser frequency is tuned. To avoid a zero beat note, the frequency of the scanning laser before hitting the fast photo detector is offset by 80 MHz with acousto-optical modulator.

Part of the scanning laser beam is attenuated and sent to the thermal beam apparatus at a right angle to the atomic beam and with polarization parallel to the atomic beam axis. Adjustment of this angle is possible by remotely controlling the collimator which is mounted on a motorized two-axis tilt stage. The RF oscillator frequency is set by a computer at specific values, and the frequency counter reading is averaged until the desired accuracy is achieved. Usually the frequency uncertainty is between 15 and 25 kHz for 100 averaged values. For better frequency resolution, longer times would be necessary to complete the scan and this would approach the limitation given by the reference laser stability which is of the order of 30 kHz/h. At each RF oscillator frequency, the fluorescence and transmission signals are read and averaged (2000 samples at 4000 samples/s) while the frequency counter averages the laser frequency difference $|\nu_{\text{Scan Laser}} \pm \nu_{\text{AOM}} - \nu_{\text{Ref. Laser}}|$. The full scan of the spectrum is repeated several times to determine possible drifts of the reference laser and check the fit accuracy. Gerginov and Tanner [1] describes the laser system in more detail.

The program outputs a data file consisting of approximately 250 points per scan. The points are separated by 500 kHz in the vicinity of the fluorescence peaks and by 10 MHz between them. The density of points is determined by the computer as it reads the beat note frequency. Each data point contains the averaged fluorescence intensity and its standard deviation, the transmitted laser intensity and its standard deviation, and the averaged beat note frequency and its standard deviation. The frequency calibrated fluorescence signal with its standard deviation is then used by the fitting program.

A typical fluorescence spectrum is shown in Fig. 4. The scanning laser excites the $F = 3$ ground state and its frequency is shifted up by $\nu_{\text{AOM}} = 80$ MHz while the reference laser is locked to the $F = 3 \rightarrow F' = 2$ transition. The laser spectrum is calibrated with the frequency counter measuring the frequency difference $(\nu_{\text{Scan Laser}} + \nu_{\text{AOM}} - \nu_{\text{Ref. Laser}})$. The laser intensity is ~ 1 μW/cm^2. The scatter in the residuals is due to noise in the scanning laser with a period comparable to or greater than 0.5 s which is not averaged by the data acquisition system. Averaging the residuals over 100 data files, we found their maximum deviation from zero is 0.25 mV, several times less than for a single file. This quantity is used to put an upper limit on the systematic uncertainty induced by these fluctuations. The theoretical peak heights up to a common constant are also shown. Similar spectra are taken with the excitation starting from the $F = 4$ ground state and a typical scan is shown in Fig. 5. The reference laser is locked to the $F = 4 \rightarrow F' = 5$ transition and the acousto-optical modulator shifts the scan laser frequency down by $\nu_{\text{AOM}} = 80$ MHz. The spectrum is calibrated with the frequency counter measuring the frequency difference $(\nu_{\text{Ref. Laser}} - \nu_{\text{Scan Laser}} + \nu_{\text{AOM}})$. Averaging the residuals for 100 scans shows a maximum deviation from zero of the order of 1 mV.

The transmission signal is also fit with the same program to find the contribution from the thermal cloud. The results are compared with the parameters found by fitting the fluorescence signal. With this method, the peak centers found by fitting are determined with an accuracy of approximately 5 kHz in a single scan. The Lorentzian part of the Voigt profile is found to be 5.5(1) MHz very close to the transitions natural width of 5.23(1) MHz. The Doppler part of the Voigt profile is 2.3(1) MHz in agreement with the prediction of 13.6 mrad from the geometrical constraints imposed by the collimator.

Another test of the model is the ratio between peak amplitudes. Because of the long term variations in the thermal beam density, it is not practical to estimate these amplitudes from different scan files. But the

Table 1
The ratios between transition probabilities – experiment and theory

Ratio	Experiment	Theory	Difference (%)
$F = 3 \rightarrow F' = 2/F = 3 \rightarrow F' = 3$	0.919(3)	20/21	3.4
$F = 3 \rightarrow F' = 4/F = 3 \rightarrow F' = 3$	0.668(1)	15/21	6.4
$F = 4 \rightarrow F' = 3/F = 4 \rightarrow F' = 4$	0.324(1)	7/21	2.7
$F = 4 \rightarrow F' = 5/F = 4 \rightarrow F' = 4$	2.142(1)	44/21	2.2

ratios between the transition amplitudes in the same file should be consistent with the theoretical transition probability ratios. An estimate for these amplitude ratios will be to compare the amplitude of each Voigt profile from the same file. The measured amplitude ratios are given in Table 1 together with the theoretical ratios calculated from the angular part of the transition probabilities. The 2.2% and 3.4% difference between the measured ratios and the theoretical transition probability ratios for $F = 3 \rightarrow F' = 2/F = 3 \rightarrow F' = 3$ and $F = 4 \rightarrow F' = 5/F = 4 \rightarrow F' = 4$ is another confirmation that we work at low laser intensities and no optical pumping takes place. The excitation of the cycling transitions doesn't transfer the ground state population to the other ground state component because of the selection rules, while for the other type of transitions, the population is entirely transferred to it after several optical cycles. The fluorescence of the cycling transition for intense laser fields is much higher than that of the other transitions for which the optical pumping depopulates the ground state. The fact that the amplitude ratios between cycling and non-cycling transitions are on the order of 3% from the theoretical value shows that the excitation doesn't redistribute significantly the ground state populations and that for these laser intensities each atom interacts on average only once with the excitation field.

The noise in the spectra is mainly due to 15 mV of AC ripple on the photo detector amplifier output, the mechanical jitter of the thermal beam with respect to the laser beam due to the vacuum system vibrations, and residual acoustic noise causing frequency fluctuations in the reference laser. A possible explanation for the slightly larger Lorentzian width as compared to the natural width is that fast noise from laser frequency jitter and mechanical vibrations are integrated by the slow response of the large area photo diode–amplifier combination. In future experiments, we plan to reduce the mechanical vibrations by sending the scanning laser to the vacuum chamber using an optical fiber that can be rigidly fixed to the apparatus. In addition, we plan to improve the reference laser stability electronically. Better acoustic isolation will also reduce the laser frequency jitter.

To study possible laser-atomic beam misalignment, we calculated the fluorescence signal for atomic beam with divergence of 7×10^{-3} rad and a laser beam sent at an angle $\alpha = ((\pi/2) + 7 \times 10^{-3})$ rad with respect to the atomic beam, which corresponds to $\theta_1 = 0$ and $\theta_2 = 7 \times 10^{-3}$ rad. We chose the model parameters close to the experimental values measured for the 6p $^2P_{3/2}$ excited state. We simulated spectra with the same amplitude and splittings as our experimental spectra. They are fitted with the same program used for data analysis and the results are shown in Figs. 6 and 7.

The upper traces show the simulated data and fit. The lower traces show the residuals. The magnitude of the residuals is on the order of 0.7% of the highest peaks, and is close to the size of our experimental residuals which are about 0.8% in a single scan. Due to the deviation from the right angle between the laser and the atomic beam, the simulated peaks are Doppler shifted as much as 1.6 MHz from their positions when the angle $\alpha = \pi/2$. Still, the splittings between the peaks are the same as the ones input into the calculation of the simulated data, with a maximum deviation of only 0.9 kHz for the highest peak in Fig. 7. This number can be used as an estimate of the systematic uncertainty coming from misalignment between the laser and the atomic beam.

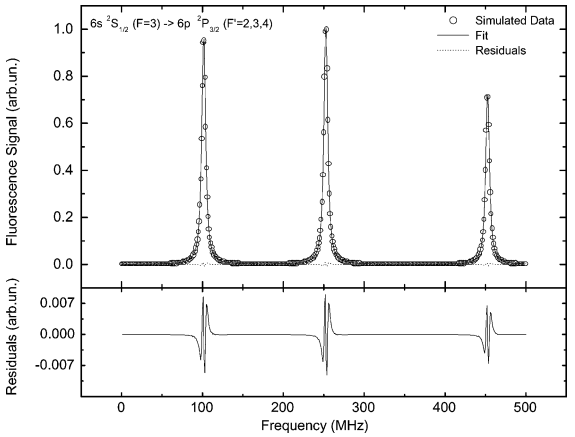

Fig. 6. Simulated spectrum for laser excitation of 6s $^2S_{1/2}(F = 3) \rightarrow 6p\ ^2P_{3/2}(F' = 2, 3, 4)$ transitions when the laser beam is sent at an angle $\alpha = ((\pi/2) + 7 \times 10^{-3})$ rad with respect to the atomic beam. The atomic beam divergence is 7×10^{-3} rad. The Lorentzian width of the transition is 5 MHz. The bottom trace shows the residuals after fitting the signal with the model described in the text.

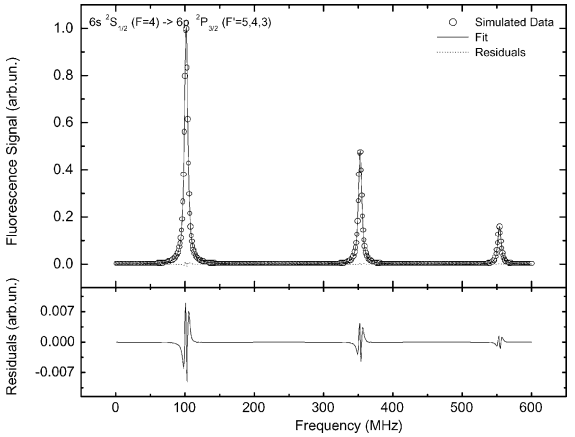

Fig. 7. Simulated spectrum for laser excitation of 6s $^2S_{1/2}(F = 4) \rightarrow 6p\ ^2P_{3/2}(F' = 5, 4, 3)$ transitions when the laser beam is sent at an angle $\alpha = (\pi/2 + 7 \times 10^{-3})$ rad with respect to the atomic beam. The atomic beam divergence is 7×10^{-3} rad. The Lorentzian width of the transition is 5 MHz. The bottom trace shows the residuals after fitting the signal with the model described in the text.

6. Conclusions

We have constructed a simple thermal atomic beam apparatus for high resolution laser induced fluorescence measurements in Cs. The atomic beam has a divergence less than 13.6 mrad as indicated by the residual 2.3(1) MHz Doppler broadening of the fluorescence signals. The fluorescence is measured with a signal to noise ratio of 500 or better. The laser system is capable of scanning over several hundred MHz with better than 25 kHz resolution. A simple theoretical model allows for the determination of frequency splittings in the measured spectra to an accuracy of a few kHz. The main sources of noise are frequency and mechanical jitter in the laser system. With the apparatus described, we plan to measure the ^{133}Cs 6p $^2P_{3/2}$ state hyperfine splittings with an accuracy several times better than in previous measurements. The atomic beam system is presently used for measurements in Cs, but it can easily be modified for measurements in other elements.

Acknowledgements

We would like to thank Steven Ruggiero, Leo Hollberg, and Jim Bergquist for their helpful discussions. Financial support for this work was provided by the Division of Chemical Sciences, Office of Basic Energy Sciences, Office of Energy Research at the U.S. Department of Energy under Grant No. DE-FG02-95ER14579 and the National Science Foundation under Grant No. PHY99-87984.

References

[1] V. Gerginov, C.E. Tanner, Opt. Commun. 216 (2003) 391.
[2] C.E. Tanner, C. Wieman, Phys. Rev. A 38 (3) (1988) 1616.
[3] J. Lloyd, in: Theory of the Hyperfine Structure of Free Atoms, first ed., Wiley–Interscience, New York, 1971.
[4] B.P. Masterson, C. Tanner, H. Patrick, C.E. Wieman, Phys. Rev. A 47 (1993) 2139.
[5] R.J. Rafac, C.E. Tanner, Phys. Rev. A 58 (1998) 1087.
[6] R. Abjean, M. Leriche, Opt. Commun. 15 (1975) 1.
[7] W. Demtröder, in: Laser Spectroscopy : Basic Concepts and Instrumentation, second ed., Springer, New York, 1996.
[8] W.H. Press, S.A. Teukolsky, W.T. Vetterling, B.P. Flannery, in: Numerical Recipes in Fortran 90, second ed., Cambridge University Press, New York, 1996.
[9] C. Chiarella, A. Reichel, Math. Comput. 22 (1968) 137.
[10] R.W. Drever, J.L. Hall, F.V. Kowalski, J. Hough, G.M. Ford, A.J. Munley, H. Ward, Appl. Phys. B 31 (1983) 97.
[11] T. Udem, J. Reichert, R. Holzwarth, T.W. Hänsch, Phys. Rev. Lett. 82 (1999) 3568.
[12] Defined by international agreement.